DEVELOPMENTAL BIOLOGY

Deciphering the ancestral mechanisms of neural regeneration through single-cell analyses of jellyfish rhopalium repair

Yongxue Li[1,2]†, Fanghan Wang[1,2]*†, Tingting Sun[1,2]†, Xiaoran Ma[1]†, Zhangyi Yu[3]†, Ziyue Xu[4], Wenhui Wang[5], Yixuan Xing[5], Saijun Peng[1], Lei Wang[1,2], Jianmin Zhao[1,2], Zhijun Dong[1,2]*

The rhopalium, an early specialized centralized nervous structure in medusozoans, exhibits a remarkable regenerative capacity after removal, offering a unique model for investigating the ancestral regulatory logic of neural regeneration. However, the cellular and molecular mechanisms underlying the process remain unknown. Here, we defined distinct stages of rhopalium regeneration in the jellyfish *Aurelia coerulea* and constructed a stage-specific cell landscape and gene regulatory networks. Notably, we identified a population of wound-induced cells that emerges rapidly postinjury and activates Wnt signaling to initiate blastema formation; cross-species comparisons revealed that this regulatory mechanism is conserved across metazoans. We further identified that retinoic acid signaling is essential for photoreceptor regeneration and ocelli reconstruction. The findings presented herein uncover the ancestral regulatory mechanisms governing neural regeneration in the early centralized nervous system, providing insights into the common evolutionary origins of neural repair across organisms.

INTRODUCTION

Neural regeneration capacity remains one of the most notable disparities in the animal kingdom (*1*). Some organisms seamlessly rebuild damaged nervous systems, restoring complex functions with remarkable precision (*2*–*5*), whereas others, including birds and mammals, struggle to repair even minor neural injuries, their repair capacity stifled by intricate cellular barriers and network complexity (*6*, *7*). This difference lies at the core of a longstanding research focus: What evolutionary principles govern the capacity for neural regeneration, and can early nervous systems that excel in this capacity illuminate the ancestral logic underlying such repair (*8*, *9*)? From planarians regenerating entire brains (*10*) to hydra rebuilding nerve nets de novo (*11*), the regenerative prowess of simpler organisms stands in stark contrast to the limitations of vertebrates. Unlocking these mechanisms extends beyond understanding biological diversity; it holds the potential to redefine approaches to neural repair, offering insights into how nature first addressed the challenge of restoring functional neural circuits.

Cnidarians, the sister group to Bilateria, provide unique insights into neural regeneration through neural architectures that balance simplicity and functionality (*5*, *12*, *13*) (Fig. 1A). Unlike the diffuse nerve nets of polyp-form cnidarians (e.g., hydra and sea anemones), medusozoans, such as scyphozoans and cubozoans, have evolved centralized sensory-motor structures termed rhopalia, which are thought to integrate photoreceptive, mechanosensory, and geosensory inputs that coordinate swimming, balance, and rhythmic activities (*12*, *14*) (Fig. 1, B and C). These structures exhibit both functional elaboration and remarkable regenerative efficacy, with certain medusozoans capable of restoring fully functional rhopalia within exceptionally short timeframes (*15*). Structural organization, coupled with a basal phylogenetic position within metazoans, makes rhopalia attractive for dissecting core regenerative mechanisms unobscured by the hierarchical complexities inherent to the nervous systems of bilaterians. Focused investigations into rhopalial regeneration thus enable the unraveling of ancestral regulatory networks that may have governed centralized nervous system repair in the last common ancestor of cnidarians and bilaterians.

Pluripotent or multipotent stem cells serve as cornerstones in organisms with robust neural regenerative capacity. Planarians deploy neoblasts to differentiate into neural lineages (*16*), annelids rely on stem cells to restore ventral nerve cords and ganglia (*17*), and cnidarians (*Hydra vulgaris*) activate multipotent interstitial cells (i-cells) to reconstruct nerve nets postinjury (*18*). However, despite having early-stage centralized nervous systems, scyphozoans lack i-cells (*19*), leaving the cellular mechanisms underpinning the precise regeneration of their rhopalia unresolved. Beyond cellular dynamics, conserved signaling networks that deeply were rooted in early metazoan evolution orchestrate regenerative processes across taxa. The Wnt, fibroblast growth factor, and retinoic acid (RA) signaling pathways have been reported to coordinate neural repair in diverse organisms, from zebrafish retinas to planarian ganglia (*20*–*23*), but their interplay with the cellular drivers of rhopalial regeneration remains poorly defined. Identifying the cellular progenitors of regenerating rhopalia and mapping the signaling networks that guide their differentiation would make it possible to illuminate the ancient regulatory blueprint underlying neural regeneration.

High-resolution analyses can systematically delineate the dynamic molecular and cellular landscapes during rhopalial regeneration, providing a critical avenue to dissecting the link between cellular origins and signaling pathways in this process. The moon jellyfish *Aurelia coerulea*, which has access to abundant high-quality genomic resources and single-cell datasets, is cultured easily under laboratory conditions, and has a transparent body structure, represents a well-suited

[1]Muping Coastal Environment Research Station, Yantai Institute of Coastal Zone Research, Chinese Academy of Sciences, Yantai, Shandong 264003, China. [2]University of Chinese Academy of Sciences, Beijing 100049, China. [3]College of Bio-Medicine and Health, Huazhong Agricultural University, Wuhan, Hubei 430070, China. [4]Department of Ocean Science, The Hong Kong University of Science and Technology, Hong Kong SAR, China. [5]School of Life Science, Yantai University, Yantai, Shandong 264005, China.
*Corresponding author. Email: fhwang@yic.ac.cn (F.W.); zjdong@yic.ac.cn (Z.D.)
†These authors contributed equally to this work.

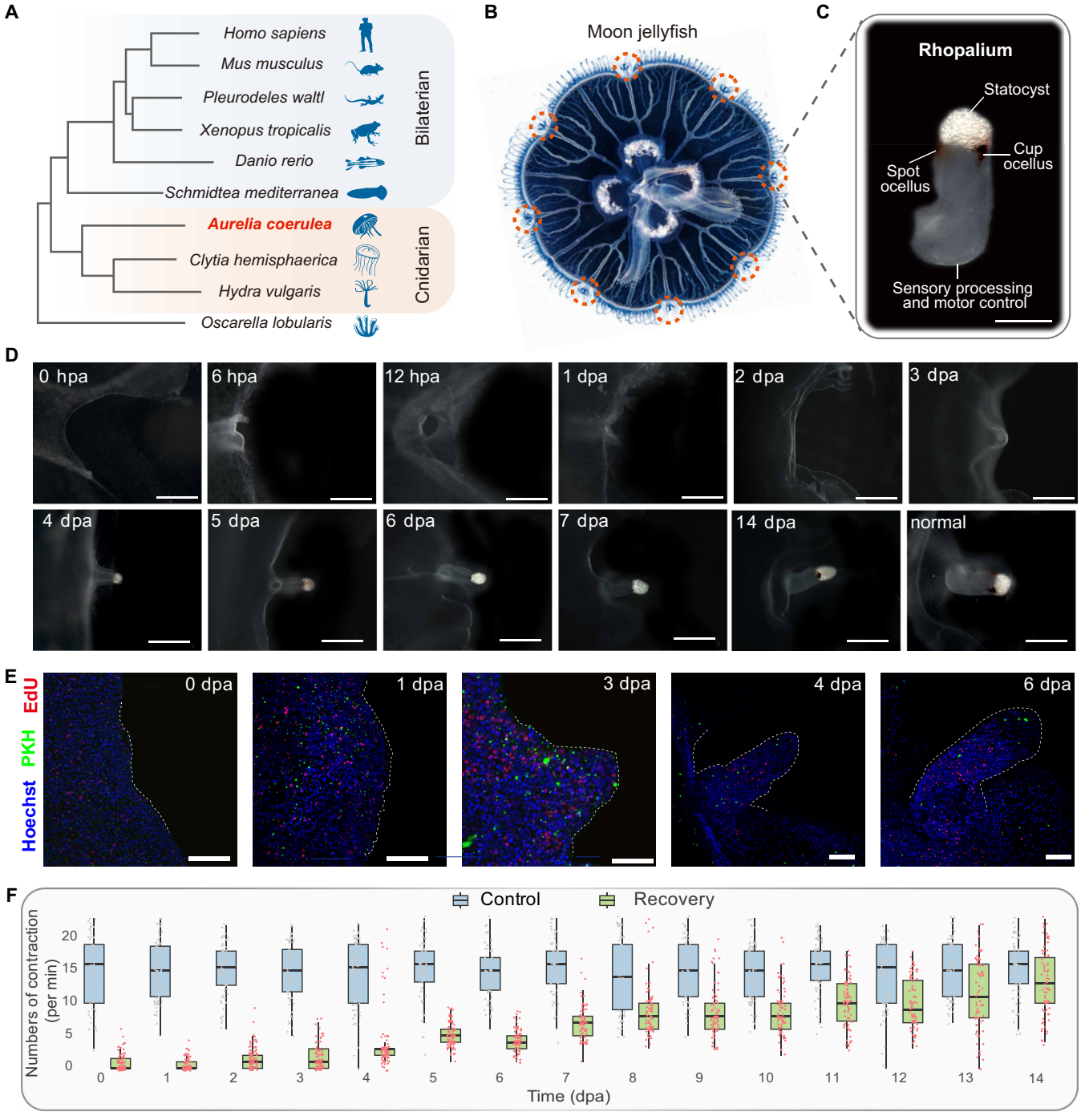

Fig. 1. Rhopalium regeneration in the moon jellyfish *Aurelia coerulea*. (**A**) Phylogenetic tree illustrating the position of the moon jellyfish *A. coerulea* among animals. (**B**) Image of the moon jellyfish *A. coerulea*. Rhopalia are marked with red circles. (**C**) Oral view of the morphological structure of the rhopalium. Scale bar, 50 μm. (**D**) Time series of the oral view showing rhopalium regeneration in *A. coerulea*. hpa, hours postamputation; dpa, days postamputation. Scale bar, 100 μm. (**E**) Cellular dynamics during the stages of rhopalium regeneration, highlighting cell migration and proliferation. PKH (green) was used to trace migrating cells, 5-ethynyl-2′-deoxyuridine (EdU; red) to label proliferating cells, and Hoechst (blue) to stain cell nuclei. Scale bars, 20 μm. (**F**) The swim contraction frequency in the jellyfish during the rhopalium regeneration process.

organism for investigating the molecular mechanisms underlying rhopalial regeneration in scyphozoans (*24*, *25*). In the present study, we systematically characterized the cellular and molecular bases of rhopalial regeneration in *A. coerulea*, combining bulk RNA sequencing, single-cell transcriptomics, cross-species comparisons, and functional validation. We identified a population of wound-induced cells (WICs) that rapidly emerges postinjury, allowing the formation of blastema through the activation of Wnt signaling. Furthermore, we found that RA signaling regulates photoreceptor regeneration, indicating its crucial role in reconstructing the photoreceptive system. Our findings establish a conceptual foundation for understanding how early centralized neuro-sensory structures regenerate in cnidarians, shedding light on the ancestral regulatory mechanisms that underpin neural repair across the animal kingdom.

RESULTS

Rhopalium regeneration and motor recovery in *A. coerulea*

Preliminary experiments systematically removed varying numbers of rhopalia from *A. coerulea* to assess their regenerative capacity. We excised one to eight rhopalia per individual and observed the complete regeneration of all the lost rhopalia, with no clear variations in the time taken for regeneration among the groups (fig. S1). On the basis of these findings, we focused on the regeneration process in *A. coerulea*, from which all eight rhopalia were removed.

Over the course of 14 days of observation, we found that rhopalium regeneration followed a distinct, staged progression (Fig. 1D). From 0 to 1 days postamputation (dpa), the wound edges shrank and folded, forming curved, white structures characteristic of the wound healing phase. Between 1 and 3 dpa, a blastema-like structure developed at the wound site. Around 3 dpa, blastema-like structures formed in 100% (40 of 40) of the wound sites. The crystal structure (statocyst) were first observed at 3 dpa and fully developed in 100% (40 of 40) of the medusae by 5 dpa, defining the statocyst formation stage (3 to 5 dpa). The photoreceptive structures (ocelli) first appeared as early as 5 dpa, and by 7 dpa, most of the regenerated rhopalia contained fully formed ocelli, defining the ocelli formation stage. From 7 to 14 dpa, the rhopalia gradually enlarged to their final size (Fig. 1D). Cell-tracking experiments and EdU labeling revealed active cell proliferation and migration across regeneration stages (Fig. 1E).

Concurrently, we observed that medusae completely deprived of all eight rhopalia lost their capacity for active swimming (Fig. 1F). Before blastema formation (0 to 1 dpa), the medusae exhibited only reflexive contractions with negligible rhythmic activity (Fig. 1F). Active swimming resumed with blastema formation (3 to 4 dpa), with an average contraction frequency of three beats per minute. This frequency increased gradually as regeneration continued, reaching 14.2 beats per minute at 14 dpa, with an average of 15.7 beats per minute observed in the uninjured control group (Fig. 1F).

Transcriptomic dynamics of rhopalium regeneration

To investigate the molecular programs governing rhopalium regeneration, we performed transcriptome sequencing across the key regeneration stages (Fig. 2A). A total of 26,729 expressed genes were identified, with 12,090 genes shared across all stages and displaying stage-specific expression patterns (fig. S2A). Gene expression similarity analysis showed that early-stage samples exhibit higher similarity, midstage samples were clearly separated, and late-stage samples shows highly similarity to the intact rhopalium (control sample) (fig. S2B). Functional enrichment and pathway analyses revealed stage-dependent differences in the activity of multiple gene ontology (GO) terms and signaling pathways during regeneration (Fig. 2B and figs. S3 and S4). In parallel, time-series clustering analysis identified multiple transcriptional modules across the regeneration process (Fig. 2C).

At the early regeneration stage (0 to 3 dpa), including wound healing and blastema formation, gene sets related to stem cell proliferation, response to wounding, extracellular matrix (ECM)–receptor interaction, as well as the Wnt and Notch signaling pathway, exhibited relatively higher pathway activity (Fig. 2B and figs. S3 and S4). At the gene level, ECM-associated genes (e.g., *Thbs1* and *Lamc1*) and Wnt genes (e.g., *Wnt2*, *Wnt3*, and *Wnt5a*) showed higher expression within this interval (Fig. 2D). Meanwhile, transcription factors such as *Hoxb4*, *Myc*, *Otx5b*, and *Pax6* displayed increased expression at specific time points within this process (Fig. 2D). During the statocyst formation stage (3 to 5 dpa), gene sets associated with otolith formation and vascular endothelial growth factor signaling showed relatively higher pathway activity (Fig. 2B and figs. S3 and S4), and the expression of the transcription factor *Nhlh1* reached its expression peak at 3 dpa, whereas that of *Pou4f3* showed increased expression at 5 dpa (Fig. 2D).

During the ocelli formation stage (5 to 7 dpa), Janus kinase–signal transducers and activators of transcription and 5′-adenosine monophosphate–activated protein kinase signaling pathways, together with gene sets associated with visual behavior and retinal cone cell development, exhibited relatively higher activity (Fig. 2B and figs. S3 and S4). Correspondingly, transcription factors (e.g., *Rax*, *Atoh7a*, and *Atoh8*) exhibited increased expression at 5 dpa within this interval, and visual behavior-related genes (e.g., *Opn4b* and *Pinopsin*) displayed increased expression at discrete time points during this period (Fig. 2D). At the maturation stage (>7 dpa), gene sets related to neuroactive ligand-receptor interaction and neurotrophin signaling displayed relatively higher pathway activity (Fig. 2B and figs. S3 and S4). Multiple neurotransmitter receptor genes (e.g., *5htrl*, *RYaR*, and *Drd2l*), together with transcription factors (e.g., *Otx1*, *Otx*, and *Foxi2*) exhibited increased expression at specific late-stage time points (Fig. 2D).

Wound-induced cell population is required for rhopalium regeneration

Dissecting cellular heterogeneity and temporal dynamics during regeneration is critical for understanding how molecular programs translate into rhopalium regeneration. On the basis of morphological assessments showing that regenerated rhopalia had attained normal structural features within 7 dpa, a single-cell transcriptomic analysis was performed across the key regenerative time points within this 7-day period, covering wound healing, blastema formation, statocyst formation, and ocelli formation (fig. S5A). After filtering, 205,747 high-quality cells were retained, and clustering identified 16 distinct clusters (Fig. 3A and fig. S5). We performed the annotation of each cluster based on previously reported marker genes (fig. S5, C and D, and dataset S1). On this basis, we found that the transcription factor *Nhlh1* was expressed predominantly in cnidocyte cluster 7 and neural cluster 5, whereas *Pou4f3* was highly expressed in sensory hair cells (cluster 8), which also showed high expression of *Myo7a*, *Otof*, and *Avil* (figs. S5C and S6A). In addition, integration of single-cell expression matrices with G protein–coupled receptor (GPCR) feature screening and phylogenetic analyses led to the identification of

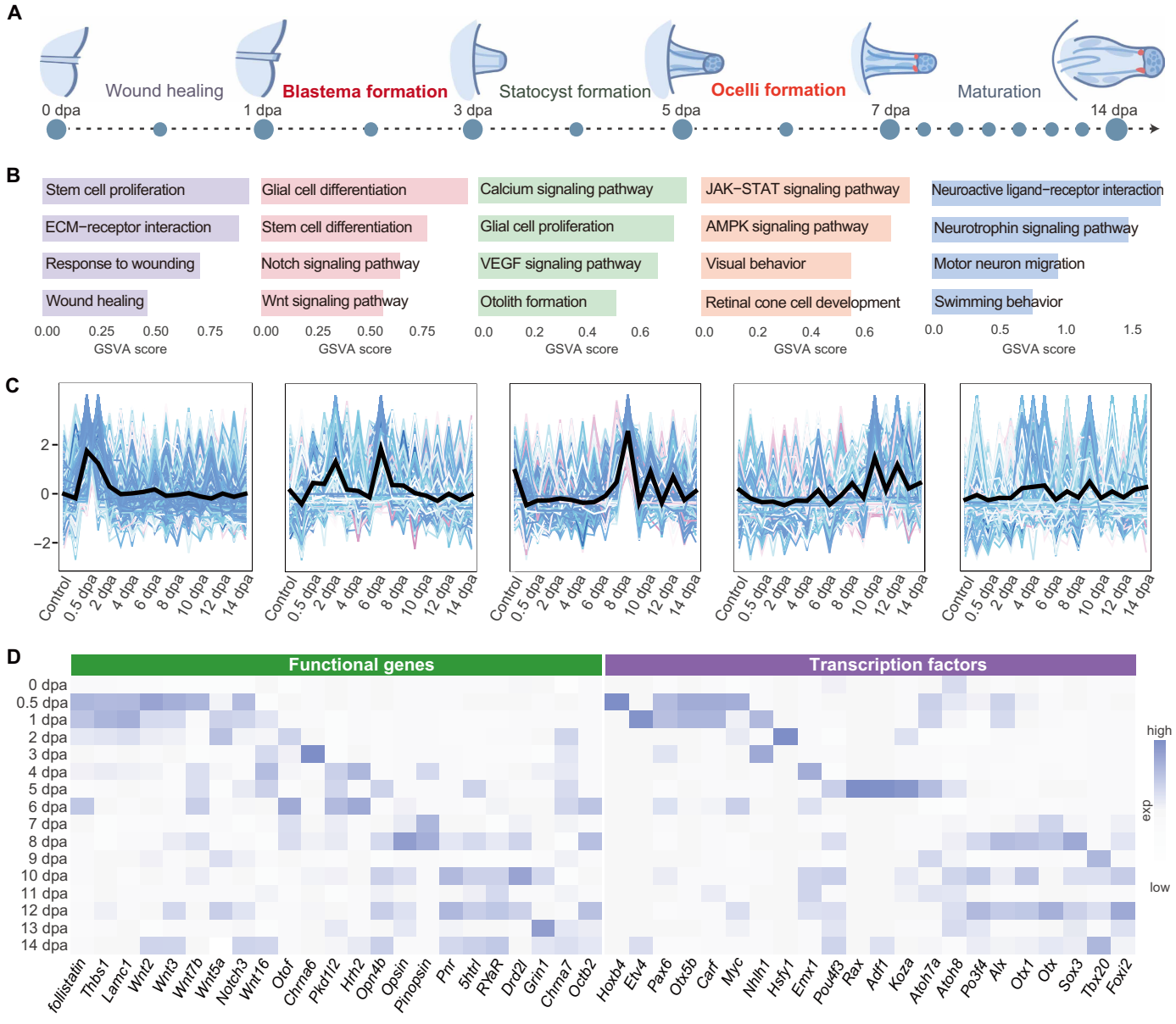

Fig. 2. Temporal bulk RNA sequencing analysis during rhopalium regeneration in *Aurelia coerulea*. (**A**) Schematic representation of the oral view of the major regenerative stages from 0 to 14 days postamputation. (**B**) GSVA analysis shows dynamic changes in the activity of GO terms and KEGG pathways during regeneration. (**C**) Mfuzz clustering analysis shows the temporal expression patterns of gene sets during rhopalium regeneration. (**D**) Heatmap showing the expression patterns of representative regeneration-related genes across different stages.

21 olfactory receptor–related genes (fig. S6B). These genes were typically expressed in only a small number of cells but displayed pronounced cell type specificity, with many showing high expression levels in neural cluster 5 (e.g., *Taar7d*, *Cnr1*, *Mc1r*, and *Htr7*) and sensory hair cell (e.g., *Adora3* and *Htr1d*) (fig. S6C). Comparative analyses across different regeneration stages revealed clear temporal regulation of olfactory-related genes (fig. S6D). Several receptor genes, including *Htr7*, *Mc1r*, *Adora2a*, and *Mshl*, were not detected at 0 dpa but became progressively expressed at later regenerative stages (fig. S6D).

Cell proportion analysis revealed that the cluster 2 peaked during blastema formation and rapidly declined thereafter (Fig. 3B and fig. S7), revealing a population of WICs that emerges specifically at the onset of regeneration. The pseudotime analysis positioned WICs at the root of the regenerative trajectory (fig. S8A). Meanwhile, WICs functioned as a signaling hub broadly interacting with other clusters (fig. S8B) and displayed transcriptional programs linked to ECM-receptor interaction, chromatin organization, and Wnt signaling pathway (Fig. 3C). The WICs further highly expressed genes associated with wound healing (*Plg* and *Col6a5*), stem cell pluripotency (*Piwi1*, *Soxf2*, and *Otx5b*), and Wnt signaling (*Fzd10*, *Wntless*, *Wnt1*, and *Wnt3*) (Fig. 3D and fig. S8C), with peak expression occurring during the wound healing stage (0 to 1 dpa) (fig. S8D). Spatial validation by in situ hybridization confirmed that *Wntless*, *Col6a5*, and

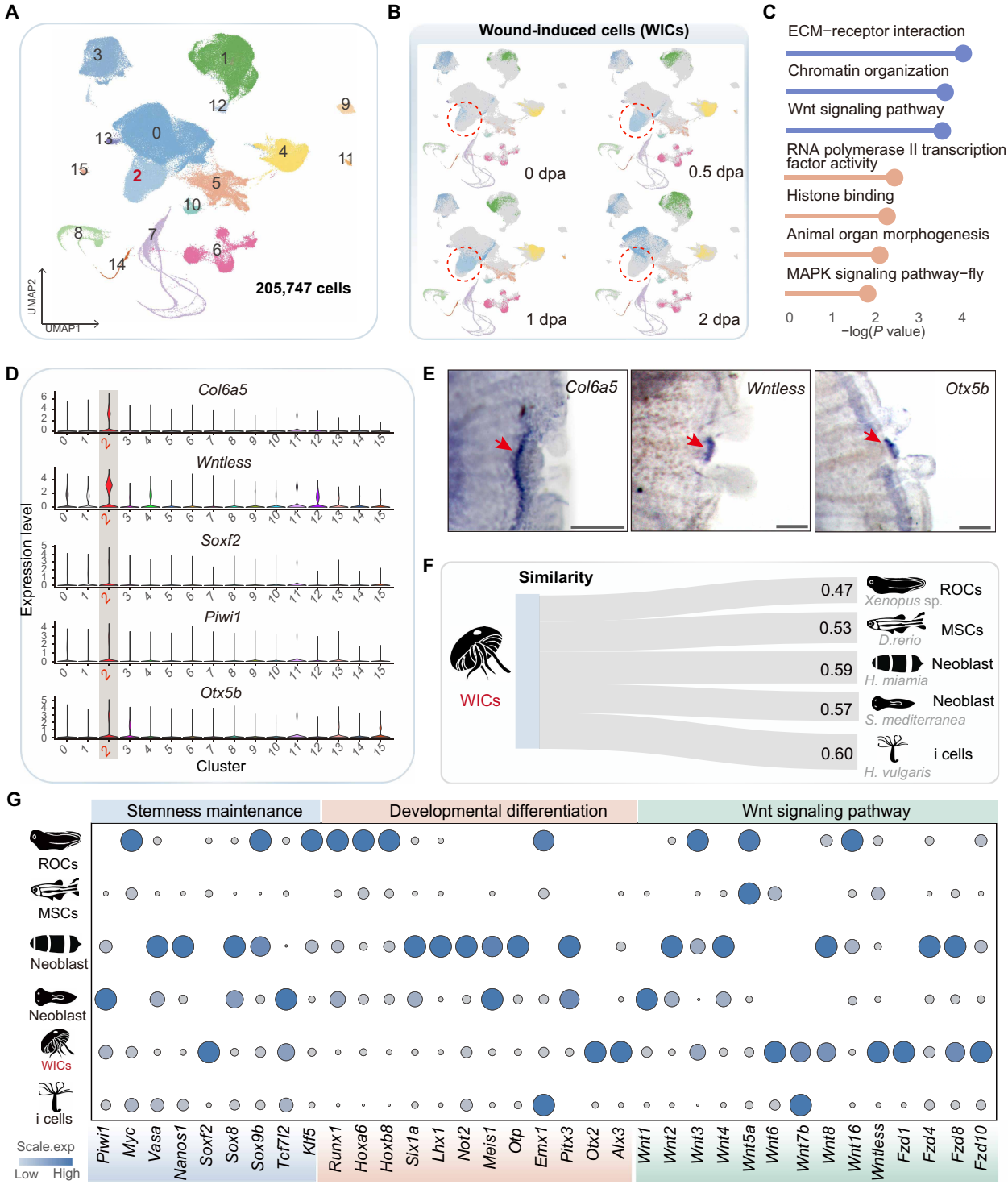

Fig. 3. Identification and characterization of a wound-induced cells (WICs) population during rhopalium regeneration. (**A**) Uniform manifold approximation and projection (UMAP) atlas of color-coded cell classes involved in rhopalium regeneration based on the single-cell RNA (scRNA) sequencing data. (**B**) UMAP distribution of cells in the early regeneration sampling stage, related to fig. S7. Colored dots represent cells from the corresponding time points, whereas gray dots represent all cells from all stages. The cell types with significant changes are marked by red circles. (**C**) Functional enrichment analysis of WICs. (**D**) VInplot displaying the expression of key marker genes in WICs. (**E**) In situ hybridization images showing the spatial expression patterns of marker genes in WICs. Blue signals represent the localization of gene expression. Scale bars, 100 μm. (**F**) Sankey diagram illustrating the similarity between WICs and known regenerative cell types across species. ROCs, regeneration-organizing cells; MSCs, mesenchymal stem cells; i-cells, interstitial cells. (**G**) Dot plot showing the similarities and differences in gene expression patterns among WICs and other early regeneration–associated cell types.

Otx5b were predominantly expressed in the blastema formation region (Fig. 3E). Subsequently, we performed gene knockdown experiments targeting WICs markers, including *Soxf2*, *Otx5b*, and *Wntless* (fig. S9A). After 4 days of treatment, knockdown of *Soxf2* or *Otx5b* resulted in a complete loss of blastema formation (0 of 16 individuals in both groups), whereas *Wntless* knockdown led to partial impairment, with blastema formation observed in a subset of individuals (4 of 16) (fig. S9B). In contrast, blastema formation occurred in the majority of control individuals (15 of 16; fig. S9B). Quantitative polymerase chain reaction (PCR) analysis further confirmed reduced expression of the targeted genes following knockdown (fig. S9C).

Cross-species comparisons revealed that WICs shared conserved molecular signatures with early regeneration-associated cell populations across metazoans, including regeneration-organizing cells in *Xenopus* sp., mesenchymal stem cells in zebrafish, neoblasts in planarians and acoels, and i-cells in *H. vulgaris* (Fig. 3F). These cells also expressed homologous genes of stemness (*Sox8*, *Vasa*, and *Sox9b*) (*26*–*28*), developmental TFs (*Runx1*, *Six1a*, and *Hoxb8*) (*29*–*31*), and Wnt signaling components (*Wntless*, *Fzd4*, and *Fzd10*) (Fig. 3G). Collectively, these results indicate that WICs are a transient cell population that functions at early stages of regeneration and is required for blastema formation.

Wnt signaling is required for WICs activation and blastema formation

To further elucidate the regulatory factors that activate and sustain WICs during early regeneration, we performed a subclustering analysis of WICs during the blastema formation stage and identified six subpopulations (Fig. 4A). These subpopulations exhibited marked stage specificity, and a pseudotime trajectory analysis revealed dynamic expression changes in key TFs (*Msx*, *Rax*, *Dlx5*, and *Runx1*) and Wnt signaling genes (*Wnt1*, *Wnt3*, *Wnt4*, *Wnt5a*, and *Wntless*) (Fig. 4, B and C). Bulk transcriptomic profiling further revealed the up-regulation of Wnt pathway genes during the blastema formation stage (Fig. 2D), implicating Wnt signaling as a key regulator of WICs state transitions during early regeneration.

To functionally validate this regulatory role, regenerating jellyfish were treated with the Wnt inhibitor IWP2 (*32*) to test whether Wnt signaling is required for WICs activation during early regeneration (Fig. 4D). After 72 hours, blastema-like structures formed in nearly all the controls (22 of 24) but in only a small fraction of the treated individuals (2 of 22) (Fig. 4D). Inhibitor treatments led to significant down-regulation of WICs marker genes *Piwi1* and *Soxf2* in WICs ($P < 0.05$) (Fig. 4E). These findings indicate that Wnt signaling is important for proper WICs activation and blastema formation during early regeneration.

Given the critical role of Wnt signaling in WICs-mediated regeneration, we next examined whether this regulatory mechanism is evolutionarily conserved. Cross-species comparative analyses focused on the early blastema formation stage across diverse regeneration models, including lizard tail, zebrafish fin, planarian body, and acoel head regeneration, revealed the up-regulation of multiple Wnt pathway homologous genes (*Wntless*, *Wnt2*, *Wnt5a*, and *Wnt6*) during this stage across species (Fig. 4F), indicating that Wnt signaling acts as an evolutionarily conserved regulator of early regenerative programs across metazoans.

To further characterize the cellular dynamics following WICs activation, we performed high-resolution reclustering of WICs-associated cell populations (Fig. 4G and fig. S10A). Integrating trajectory inference results from Monocle3 and Slingshot, we found that WICs primarily give rise to two major differentiation branches (Fig. 4G and fig. S10B). One branch progressed from WICs toward the NPs-3 (neural progenitor cells-3) population and extended further to an unclassified cluster, characterized by high expression of *Dlx5* and elevated *Otx1a* expression during the early transition stage. The second branch showed the differentiation trajectory of WICs toward NPs-1/NPs-2. Along this trajectory, cells sequentially undergo two key stages: NPs-1 and NPs-2. During differentiation into the NPs-1 stage, transcription factors associated with NPs, including *Sox9b*, *Foxb1*, *Otx2*, and *Drgx*, showed high expression, and after entering the NPs-2 stage, whereas at the NPs-2 stage, *Hoxa4* and *Foxi2* expression increased (Fig. 4G). From the NPs-2 node, this trajectory branched further into three neural subtypes, marked by increased expression of distinct transcription factors, including *Atoh7a* for NCs-1, *Klf6* and *Foxl2* for NCs-2, and *Lmx1b.1* for NCs-3, respectively (Fig. 4G).

Stage-specific transcriptional programs drive photoreceptor cell regeneration

Previous morphological observations confirmed that the photoreceptive structures (ocelli) within the rhopalium of *A. coerulea* are regenerative (Fig. 1D). Transcriptomic profiling showed the significant up-regulation of the photoreceptor gene *Opsin* (*33*, *34*) during ocelli regeneration (Fig. 2D), indicating this process involves photoreceptor cell regeneration. At the single-cell level, *Opsin* expression was initially detected in a small subset of neural cells (cluster 21), reflecting photoreceptor-lineage cells (PLCs) (fig. S11, A and B). A subclustering analysis of cluster 21 identified six subclusters (Fig. 5A, fig. S11B, and dataset S1). Among these, one subcluster expressed the pluripotency/stemness marker *Myc* (*35*), which, along with neural progenitors (NP) markers such as *Otx1a* (*36*) and *Fzd1* (*37*), was annotated as an NP cell (Fig. 5A and fig. S11C). Photoreceptor-lineage cluster 1 (PLC1) showed the highly specific expression of the photoreceptor gene *Opsin*, and fluorescence in situ hybridization confirmed that *Opsin* was mainly localized to the ocelli region (Fig. 5B), indicating that PLC1 represents photoreceptor cells. A cellular proportion analysis revealed that PLC1 emerged as early as 0.5 dpa and expanded progressively thereafter (Fig. 5A and fig. S11D). In addition, *Opsin* expression was first detected at 4 dpa, and multiple key effector genes involved in phototransduction (e.g., *Tle4*, *Pde6d*, *Pde11a*, *Trpa1*, and *Adcy3*) were predominantly became detectable during the 3 to 4 dpa stage (Fig. 5C and fig. S12). These results indicate that photoreceptor cells and their photoreception-related molecular programs can be re-established during rhopalium regeneration.

Next, we reconstructed a transcriptional trajectory delineating the differentiation of NPs into photoreceptor cells (Fig. 5D). Functional enrichment analyses along this trajectory revealed dynamic changes in pathways related to neural development and photoreceptive function (Fig. 5E). Notably, phototransduction, retinol metabolism, axon guidance, and neurotrophin signaling pathway were markedly activated during photoreceptor cell regeneration (Fig. 5F), suggesting their roles in establishing photoreceptive functionality. In addition, genes involved in RA metabolism and biosynthesis (*Ugt*, *Bco1*, *Rdh8*, *Rdh12*, *Aldh*, and *Aldh1a*) exhibited distinct temporal expression dynamics along the pseudotime (Fig. 5G), pointing to their potential regulatory roles in photoreceptor regeneration.

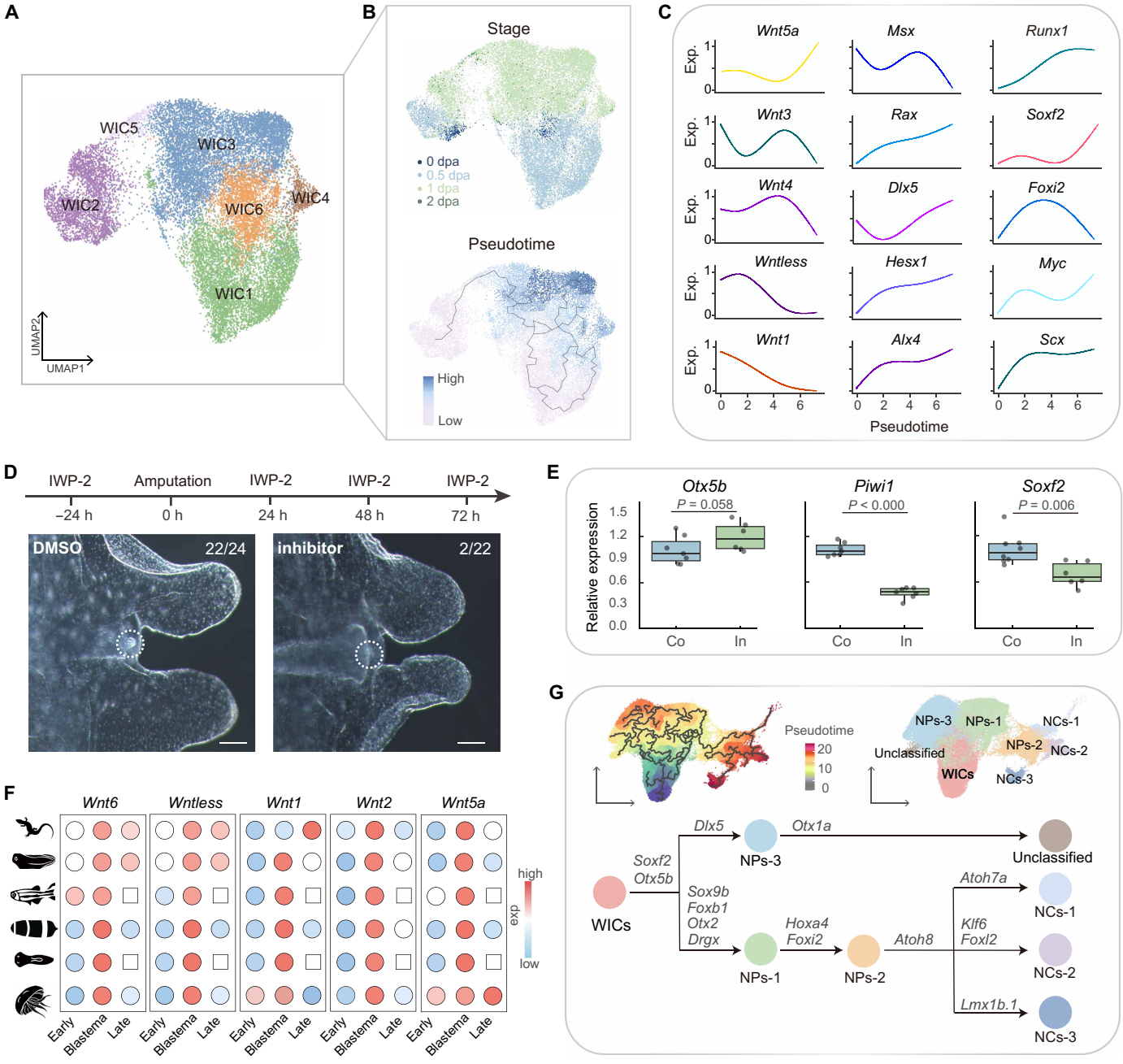

Fig. 4. Wnt signaling drives WICs activation and blastema formation during early rhopalium regeneration. (**A**) UMAP visualization of the subclustering analysis of WICs during blastema formation. (**B**) Stage-wise distribution (top) and pseudotime inference (bottom) of WICs. (**C**) Expression dynamics of key genes along the WICs trajectory (**D**) Functional inhibition of the Wnt signaling pathway. Top: Schematic of the experimental workflow. Bottom: Morphological comparison of different treatment groups, with numbers in the upper right corner (e.g., 22 of 24 and 2 of 22) indicating the number of wound sites with blastema formation among the total wound sites tested. White-circled region marks the site of rhopalium regeneration. Scale bars, 50 μm. (**E**) Box plot showing the expression of WICs marker genes in different treatment groups. Co, control group; In, inhibitor group. (**F**) Dot plot displaying the expression trends of homologous Wnt-related genes across species during blastema formation. The "□" symbol denotes data that are not available in public repositories. (**G**) Trajectory reconstruction of WICs differentiation during regeneration. The upper panels present pseudotime ordering inferred by Monocle3 (left) and show UMAP visualization of WICs-associated cell populations following high-resolution reclustering (right). The bottom schematic summarizes the inferred differentiation trajectories originating from WICs, reconstructed by integrating Monocle3 and Slingshot analyses, corresponding to fig. S10B. Transcription factors displayed along each arrow represent genes that are highly expressed during the corresponding transitional states along the trajectory. NPs, neural progenitor cells; NCs, neural cells.

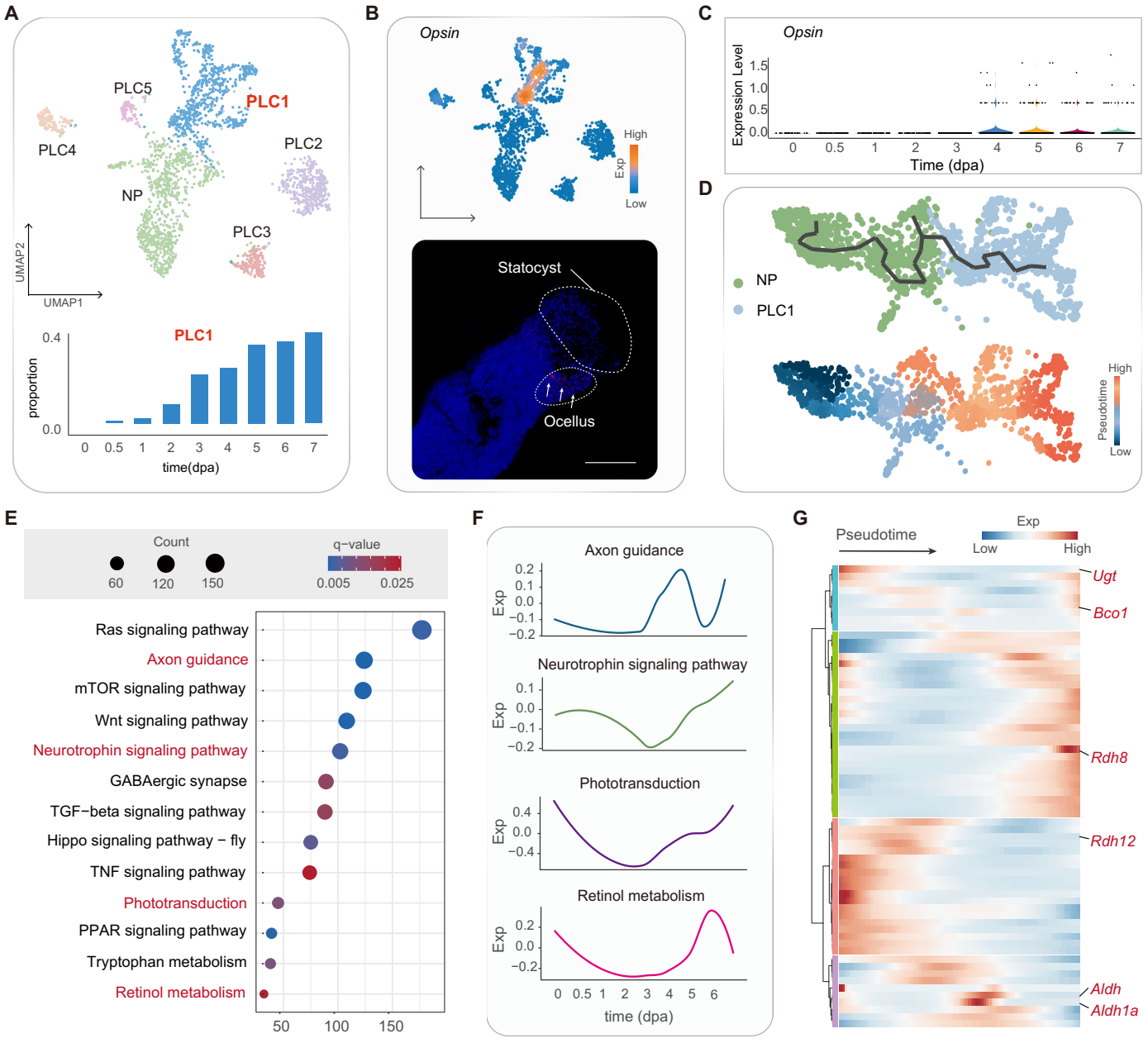

Fig. 5. Transcriptional dynamics of photoreceptor cells during regeneration. (**A**) UMAP visualization of PLCs following subclustering (top) and proportional changes of the PLC1 population across regeneration stages (bottom). (**B**) *Opsin* expression shown by feature plots (top) and whole-mount fluorescence in situ hybridization (FISH) confirming *Opsin* localization in the ocelli region (bottom). Scale bar, 50 μm. (**C**) Violin plots showing the temporal expression of *Opsin* across regeneration time points. (**D**) Pseudotime trajectory of PLCs showing the transition from NP to PLC1. (**E**) Dot plot of the enriched pathways along the pseudotime trajectory. (**F**) Module scores of the temporal activation dynamics of key pathways across regeneration time. (**G**) Heatmap showing the expression dynamics of genes along the pseudotime.

RA signaling regulates photoreceptor cell regeneration and ocelli formation

To further explore the functional role of RA signaling in photoreceptor cell regeneration, we conducted pharmacological perturbation experiments 2 days after rhopalial removal (corresponding to the blastema formation stage). Jellyfish were treated with dimethyl sulfoxide (DMSO; control), 4-Diethylaminobenzaldehyde (DEAB), a retinaldehyde dehydrogenase inhibitor that blocks RA synthesis (*38*), and DEAB supplemented with exogenous RA (DR group) to assess the role of RA signaling in photoreceptor cell regeneration (Fig. 6A). After 72 hours of treatment, DEAB treatment delayed the regeneration of both the ocelli and the statocysts significantly ($P < 0.05$), whereas DR treatment promoted significant ocelli regeneration ($P < 0.05$) (Fig. 6B). Morphological observations showed that DEAB treatment resulted in reduced rhopalium size and was accompanied by a pronounced delay in ocelli formation, whereas the DR group exhibited markedly enlarged rhopalial morphology and ocelli size (Fig. 6C).

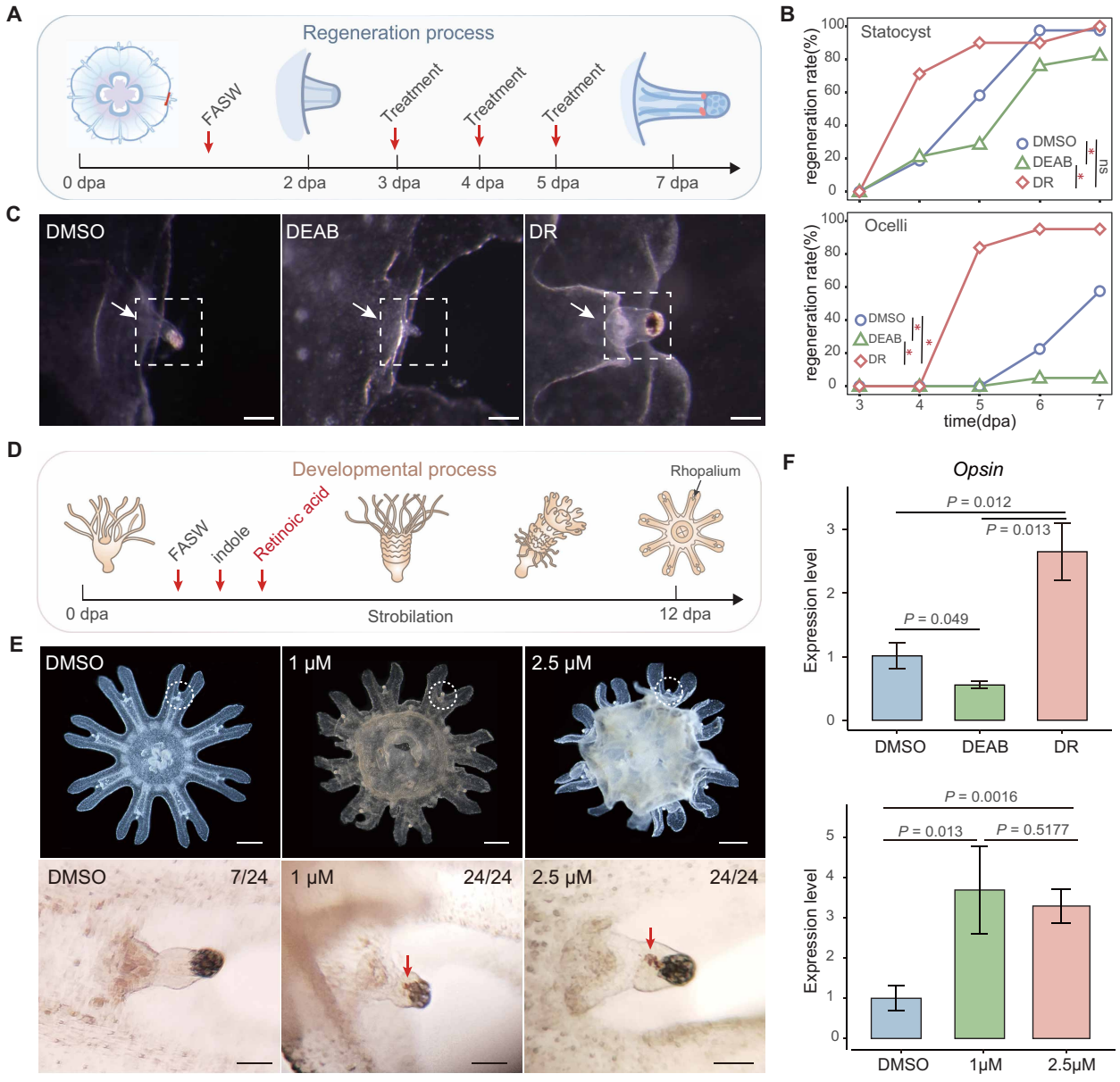

Fig. 6. RA signaling regulates photoreceptor cell regeneration and ocelli formation. (**A**) Schematic of the pharmacological perturbation experiment. Jellyfish were treated with DMSO (control), DEAB (RA synthesis inhibitor), or DEAB plus exogenous RA (DR, rescue group) 2 days after rhopalium removal. (**B**) Regeneration rates of statocysts (top) and ocelli (bottom) under different treatments ($n = 10$). *$P < 0.05$. (**C**) Images of regenerated rhopalia at 7 dpa under different treatment conditions. Arrows indicate the location of regenerated rhopalia. Scale bars, 50 μm. (**D**) Schematic overview of pharmacological manipulation of RA signaling during normal ephyra development. (**E**) Representative images showing morphological changes and ocelli formation in control and RA-treated ephyrae, with numbers in the upper right corner indicating the number of rhopalia with ocelli formation among the total ocelli tested. White-circled region marks the site of rhopalium. White scale bars, 500 μm; black scale bars, 20 μm. (**F**) Quantitative PCR analysis of *Opsin* expression under different treatment ($n = 3$).

Given the prominent effects of RA signaling on ocelli regeneration, we investigated whether RA also influences ocelli formation during normal development, by performing pharmacological perturbations during ephyra (juvenile medusa) development (Fig. 6D). All individuals formed statocysts within 10 days across all treatment groups (fig. S13). At 12 days post-treatment, compared with controls, RA-treated ephyrae exhibited pronounced morphological alterations, including enlarged lappets (Fig. 6E). At higher RA concentrations (2.5 μM), released ephyrae displayed conjoined morphologies accompanied by further expansion of the lappets (Fig. 6E). Examination of ocelli development revealed that all RA-treated ephyrae formed discernible ocelli structures (24 of 24) (Fig. 6E). In addition, quantitative PCR analysis showed that *Opsin* expression was reduced significantly in regenerating jellyfish following DEAB treatment (Fig. 6F). By contrast, during normal development, RA treatment led to a marked up-regulation of *Opsin* expression compared with controls (Fig. 6F).

DISCUSSION

The regeneration of centralized neural-sensory structures represents a defining challenge in understanding the evolutionary origins of tissue repair, with profound implications for deciphering how metazoans first acquired the capacity to restore complex functional systems (*6*, *39*). Although most bilaterians display limited or no ability to regenerate sensory structures (*40*), our study demonstrates that the jellyfish *A. coerulea* can fully reconstruct rhopalia, the integrative sensory-motor centers (*41*). This regenerative process involves blastema formation, after which subsequent tissues regenerate in an order and temporal pattern that is consistent with normal development, while sustained cell proliferation and cell migration are maintained throughout the process. This regenerative mode is consistent with regeneration processes reported in several highly regenerative species (e.g, hydra, planarian, and zebrafish) (*11*, *40*). By integrating bulk and single-cell transcriptomics with functional perturbation assays, we reconstructed the cellular and molecular patterns during rhopalia regeneration. We identified a transient population of WICs that initiate regeneration through Wnt signaling and further reconstructed the transcriptional trajectory of photoreceptor cell regeneration, which was found to be regulated by an RA-dependent transcriptional cascade. These results define a stepwise program for rebuilding centralized sensory structures and highlight conserved regulatory strategies that may underlie neural regeneration across diverse animal lineages.

Regenerative capacity is typically supported by a population of regeneration-driving cells (*40*), with distinct cell populations underpinning repair across taxa that planarians rely on resident pluripotent neoblasts (*10*, *42*), hydrozoans on i-cells (*43*), and vertebrates on tissue-specific stem or progenitor cells (*1*, *7*, *40*). In contrast, although early morphological studies have reported the presence of undifferentiated cells in nonhydrozoan cnidarians (e.g., Cubozoans) (*14*, *15*), a resident pluripotent stem cell population equivalent to *hydra* i-cells has not been clearly identified (*19*), leaving the cellular basis of their robust regenerative capacity unresolved. In the present study, we identified a population of WICs that transiently emerges and becomes enriched at the onset of rhopalium regeneration in the scyphozoan *A. coerulea*; these WICs play a nonredundant role in blastema formation, as gene knockdown of WICs-specific markers abrogates or impairs this process. At the transcriptional level, WICs exhibit pronounced similarities to pluripotent stem cells across metazoans including planarian neoblasts, and *hydra* i-cells coexpressing a core set of evolutionarily conserved stemness-associated genes (*Piwi1*, *Nanos*, and *Vasa*) (*27*, *44*, *45*) and Wnt signaling components. This suggests that nonhydrozoan cnidarians may harbor cell populations characterized by stemness-related molecular signatures that are mobilized postinjury to drive regeneration, representing a convergent or basic strategy for tissue repair. Furthermore, after excluding significant effects of pharmacological treatment on overall cell viability (fig. S14), we observed that inhibition of Wnt signaling reduced the expression of WICs marker genes markedly and disrupted blastema formation substantially, indicating that Wnt signaling is specifically required for WICs activation or proliferation and function during regeneration initiation. This regulatory role aligns with conserved functions of Wnt signaling in planarian tail regeneration (*46*), zebrafish caudal fin regeneration (*47*), and tadpole early-stage limb regeneration (*48*). Collectively, these observations suggest that Wnt signaling may act as a deeply conserved regenerative switch that activates regeneration-associated cell populations to initiate blastema formation, highlighting a core regulatory module inherited from the last common ancestor of cnidarians and bilaterians. In addition, single-cell trajectory analyses allowed us to infer preliminarily putative differentiation trajectories and potential fates of WICs, revealing stage-specific activation of multiple transcription factors along the regenerative continuum. However, owing to the current lack of well-established genetic manipulation and lineage-tracing tools in jellyfish, these inferred trajectories could not yet be experimentally validated in vivo.

Jellyfish represent one of the earliest animal lineages to evolve specialized photoreceptive structures, with their rhopalial ocelli integrating light signals to coordinate motor responses (*49*, *50*). Our study demonstrated that these ocelli are fully regenerative and reconstruct the differentiation trajectories of photoreceptor cell types at single-cell resolution, revealing RA signaling as a pivotal regulator of this process. Notably, while RA was shown to regulate *Opsin* expression and promote ocelli development, we also observed that different RA doses markedly influence overall ephyrae morphology. Pronounced morphological alterations were detected both in regenerating rhopalia and in rhopalia formed during normal development. Similar dose-dependent effects of RA on patterning and regeneration have been reported in other animal systems, including regeneration and pattern formation in planarians (*51*, *52*), anterior-posterior hindbrain patterning in *Xenopus* embryos (*53*), and cranial ganglion formation in zebrafish embryos (*54*). In addition, recent studies have shown that exogenous supplementation with appropriate levels of RA can reprogram the fate and transcriptional programs of key regenerative cells, enabling the reconstruction of cartilage and neural tissues in adult mouse ear pinna wounds that otherwise lack regenerative capacity (*55*). Our observations indicate that RA signaling, as a conserved developmental regulatory signal, is capable of modulating the initiation hierarchy of developmental signaling programs in a dose-dependent manner during both regeneration and development. These parallels spanning cnidarians to vertebrates also highlight that its role in sensory structure regeneration and patterning is an ancestral trait pre-dating the divergence of cnidarians and bilaterians, underscoring how conserved developmental pathways were co-opted for regenerative processes throughout evolution.

The single-cell transcriptomic atlas of rhopalium regeneration provides initial insights into the molecular and functional organization of early centralized sensory structures. We identified a specific cell cluster in which the transcription factor *Pou4f3*, which is essential for vertebrate hair cell differentiation and normal hearing (*56*), is coexpressed with gene markers of vertebrate sensory hair cells (*Myo7a*, *Otof*, and *Avil*) (*57*–*59*), suggesting a degree of molecular conservation between jellyfish sensory hair–like cells and vertebrate hair cells, despite their profound structural differences. However, currently, direct evidence demonstrating bona fide auditory perception in jellyfish is lacking, and whether this molecular resemblance corresponds to functional sensory perception remains to be determined. In addition, we uncover a small subset of neural cells specifically expressing olfactory receptor–related genes, with some olfactory-related genes being activated only during regeneration, indicating the presence of neural types potentially associated with chemosensory functions and suggesting that rhopalium regeneration may involve the establishment or reconstruction of olfactory-related neural programs. These findings challenge the view of rhopalia as quite simple sensory structures, particularly in cubomedusae where they exhibit considerable complexity (*14*), and highlight the utility of jellyfish as models for understanding the evolutionary origins of sensory system organization.

Behavioral recovery during rhopalium regeneration, marked by the gradual restoration of swimming contraction frequency, further links cellular and molecular events to functional outcomes. Putative swimming pacemakers are a cluster of giant neurons in the proximal region of the rhopalium, whose action potentials trigger bell muscle contractions one to one (*60*). Previous studies in the box jellyfish *Tripedalia cystophora* have shown that rhopalium regeneration restores pacemaker-like electrical signals, with firing frequency rising gradually (*15*). Further, in scyphozoans, multiple pacemakers are thought to increase the frequency and regularity of swim contractions (*61*). The gradual recovery of swimming frequency in our observation is therefore functionally consistent with classical models of pacemaker network regulation and suggests that rhopalium regeneration may involve reconstruction of pacemaker-related functional units, although direct verification of pacemaker neuron regeneration remains limited owing to the lack of definitive molecular markers. Hence, future efforts should focus on establishing genetic manipulation platforms in jellyfish, including gene editing, transgenesis, lineage-tracing technologies, and integrating them with regenerative atlases and functional validation. These will enable systematic dissection of the cellular composition and functional organization of early centralized nervous systems, and will provide deeper insights into how centralized neural organs are rebuilt and progressively regain function during regeneration.

MATERIALS AND METHODS

All animal experimentation performed did not require Institutional Animal Care and Use Committee approval.

Animal husbandry

Medusae from *A. coerulea* were maintained in 60-liter jellyfish cultivation tanks at the Muping Coastal Environment Research Station, Yantai Institute of Coastal Zone Research, Chinese Academy of Sciences. The medusae were kept in filtered artificial seawater [FASW; 0.22 μm, salinity of 30 parts per trillion (ppt)], with one-third of the medium replaced every 2 days to maintain water quality. A controlled light-dark cycle of 8:16 hours was applied using a standard timer. The medusae were fed daily with freshly hatched *Artemia* nauplii.

Rhopalial amputation and subsequent regeneration

To investigate the regeneration of rhopalia, 100 medusae, each having eight rhopalia, were selected. All the rhopalia were surgically removed using a sterile scalpel, and the medusae were subsequently returned to the cultivation tanks. Regeneration and contraction frequency were monitored over a 14-day period, during which samples were collected for bulk RNA and single-cell RNA sequencing (scRNA-seq) analyses. During cultivation, the medusae were maintained at 15°C in FASW (salinity, 30 ppt), with one-third of the water replaced every 2 days. The medusae were fed freshly hatched *Artemia* nauplii every 3 days.

Locomotor behavior monitoring

Locomotor behavior during rhopalia regeneration was assessed by measuring the pulse rate of the medusae bell. After the complete removal of all rhopalia, 15 medusae were transferred to a cultivation tank under controlled conditions. The locomotor behavior of the medusae was continuously recorded for 5 min daily using a high-resolution video recording system. The pulse rate of each medusa was calculated as the number of bell contractions per minute. Both the control group and the experimental group consisted of 15 healthy adult medusae. Throughout the experiment, the same rearing conditions and observation period were applied to both groups to eliminate interference from differences in sample size and environmental factors on the experimental results. This measurement was performed daily over a period of 14 days to monitor changes in swimming behavior during the regeneration process.

PKH and EdU labeling

To simultaneously track cell migration and assess cell proliferation during rhopalia regeneration, medusae were labeled with both PKH67 dye (Fluorescence, China) and EdU cell proliferation assay kit (Beyotime, Jiangsu, China). In brief, medusae (2 to 3 cm in diameter) were first incubated with PKH67 dye at a final concentration of 20 μM in FASW for 2 hours at 19°C in the dark to achieve uniform membrane labeling. After thorough rinsing with FASW to remove excess dye, all rhopalia were removed surgically using sterile scalpels. For EdU labeling, medusae were transferred to 100-ml glass beakers containing FASW supplemented with 150 μM EdU and incubated for 2 to 4 hours at 19°C. Following incubation, medusae were washed thoroughly with fresh FASW and processed for EdU detection according to the manufacturer's instructions. Nuclear staining was performed using Hoechst 33342 with overnight incubation at 4°C in the dark. The fluorescence imaging of different samples was conducted using a confocal microscope (Olympus IX83).

Transcriptome sequencing and analysis

Regenerating rhopalial tissues were collected from intact controls and at 0, 0.5, 1, 2, 3, 4, 5, 6, 7, 8, 9, 10, 11, 12, 13, and 14 dpa, as detailed in table S1. For each time point, the rhopalial region was defined as a standardized segment of the bell margin encompassing the original rhopalium excision site, including the regenerating regions and the surrounding tissues within a ~1 mm radius. Each sample consisted of tissue pooled from five to six equivalent excision sites. All biological replicates were derived from independent individual medusae, with three biological replicates per stage. Total RNA was extracted using the Illustra Polyphenol Polysaccharide Plant Total RNA Extraction Kit (ZOMANBIO, Beijing, China) according to the manufacturer's protocol. RNA quality was assessed, and only samples with OD260/280 $\geq$ 1.8, OD260/230 $\geq$ 1.0, and RNA integrity number $\geq$8 were used for downstream sequencing.

Libraries were sequenced on an Illumina NovaSeq 6000 platform (2 × 150 bp read length) using triplicate mRNA samples per condition. Raw paired-end reads were processed to remove adapters, low-quality sequences, and reads shorter than 50 bp using SeqPrep and Sickle with default parameters. Clean reads were aligned to the reference genome (BioProject: PRJNA1048363) using HISAT2 and assembled with StringTie based on a reference-guided approach. All unigenes were assigned against the National Center for Biotechnology Information (NCBI) Non-Redundant Protein Sequence Database (BLASTP, e-value $\leq 10^{-5}$), SWISS-PROT Dataset and GO Database. Gene expression was calculated using the transcripts per million (TPM) method.

Fuzzy c-means clustering

Normalized TPM values were used as input for the Mfuzz (*62*) to group genes based on their expression dynamics. Following the standard pipeline, soft clustering was performed using the fuzzy c-means

algorithm. The optimal fuzzifier parameter ($m = 1.25$) and cluster numbers were selected to minimize overlap between clusters, yielding good resolution for both developmental and regenerative processes. Gene Set Variation Analysis (GSVA) (*63*) and ClusterProfiler (*64*) were used to identify enriched GO terms and Kyoto Encyclopedia of Genes and Genomes (KEGG) pathways, providing insights into the functional and pathway-level implications of the gene expression dynamics.

Preparation of cell suspensions

For the scRNA-seq library preparation, regenerating rhopalia were collected at nine time points spanning 0 to 7 dpa, covering the major stages of wound healing, blastema formation, statocyst formation, and ocelli formation (0, 0.5, 1, 2, 3, 4, 5, 6, and 7 dpa; detailed in table S2) and washed twice in Ca^{2+}- and Mg^{2+}-free FASW [CMFASW; NaCl (25 g/liter), KCl (0.8 g/liter), and $NaHCO_3$ (0.04 g/liter); pH 8.0]. The samples were immediately sliced into small fragments and transferred to a centrifuge tube containing 3 ml of digestive buffer [dispase II (3.6 mg/ml) and collagenase III (1.25 mg/ml) in CMFASW]. Tissues were dissociated at room temperature for ~20 min with occasional stirring. Once most of the tissues had dissociated into single cells (as observed microscopically), enzymatic digestion was terminated by adding fetal bovine serum to a final concentration of 8% (v/v). The single-cell suspension was then centrifuged at 650*g* for 8 min at 4°C, resuspended in prechilled CMFASW, and passed through a 40-μm cell strainer (Falcon; Corning, NY, USA). The cell suspension at each regeneration time point was prepared by pooling regenerating regions from three independent medusae at the same stage.

scRNA-seq library preparation, sequencing, and count matrix generation

Low concentrations of Calcein AM (2 mM) and Draq7 (0.3 mM) were used to assess cell viability with the BD Rhapsody system (BD Biosciences, Franklin Lakes, NJ, USA). Only cell suspensions with >90% viability were used for cell capture. The BD Rhapsody system was used for single-cell capture and library construction. The libraries were quantified using a Qubit high-sensitivity DNA assay (Thermo Fisher Scientific, Waltham, MA, USA). Sequencing was performed using the Illumina NovaSeq 6000 platform with 150 bp paired-end runs (Illumina, San Diego, CA, USA). Fastq files were processed using the BD Rhapsody WTA Analysis Pipeline (version 1.2) on Seven Bridges (https://sevenbridges.com/) following the manufacturer's guidelines. Reads were mapped onto the *Aurelia* genome (BioProject: PRJNA1048363).

Data quality control, integration, and analysis

UMI count matrices were processed with the R package Seurat (version 5.1.0) (https://satijalab.org/seurat/). To remove ambient RNA contamination and low-quality cells, the transcriptomes were filtered for each time-course sample as follows: (i) cells with fewer than 200 expressed genes were discarded; (ii) only genes expressed in at least three cells in each dataset were considered; and (iii) cells were filtered on the basis of total UMI counts, excluding the cells with excessively low (<300) or high (>10,000) UMI counts. The R package DoubletFinder (*65*) was used to identify putative doublets. To compare the differences in cell types during different stages of regeneration, quality-filtered datasets of different recovery stages were merged in Seurat following a standard analysis pipeline. We used FindNeighbors and FindClusters to generate cell clusters and identified cluster-specific gene expression signatures using the FindAllMarkers function. The R packages Monocle 3 (*66*), Slingshot (*67*), and Monocle 2 (*68*) were used to infer cell differentiation trajectories. The R package CellChat (*69*) was used to identify intercellular communication and statistically predict receptor-ligand pairs.

RNA interference

RNA interference experiments were performed using double-stranded RNA (dsRNA) synthesized with an in vitro T7 transcription kit (Takara, Japan) according to the manufacturer's instructions. Gene-specific dsRNAs were designed by SiDirect (version 2.1; https://sidirect2.rnai.jp/), and an enhanced green fluorescent protein plasmid-derived dsRNA was used as a negative control. For dsRNA delivery, dsRNA was complexed with a nucleic acid transfection reagent (RFect Prime, Baidai Biotech, China) following the manufacturer's protocol. In brief, the dsRNA-transfection reagent complexes were prepared in sterile conditions and subsequently diluted in FASW before animal treatment.

For each experimental group, four juvenile medusae (approximately 1 cm in diameter), each bearing eight rhopalia, were used. After removing four rhopalia from each medusa, the medusae were immediately transferred to 3 ml of FASW containing 10 μg of dsRNA-transfection reagent complexes, and then cultured in 12-well cell culture plates at 15°C. The FASW containing dsRNA-transfection reagent complexes was refreshed daily, and freshly hatched *Artemia* nauplii were fed every 2 days. Primer sequences used for dsRNA synthesis and quantitative PCR are listed in table S3.

Olfactory receptor gene identification and phylogenetic analysis

To identify olfactory receptor genes, we first screened potential GPCR genes based on MAKER annotation files derived from single-cell transcriptomic data. We then predicted the protein domains of these GPCRs using the InterPro database (https://ebi.ac.uk/interpro/). Genes with clearly identifiable olfactory receptor–specific domains were considered highly likely to be olfactory receptors. To identify and validate the putative olfactory receptor genes in *A. coerulea*, a phylogenetic tree was constructed to determine whether these candidates cluster with known olfactory receptors from other species like *Branchiostoma floridae*, *Homo sapiens*, and *Danio rerio*. The analysis included gonadotropin-releasing hormone receptors (GnRHR) and opsin genes from various species (*B. floridae*, *H. sapiens*, *D. rerio*, *Argopecten irradians*, *Ciona intestinalis*, *Ylistrum balloti*, and *Lethenteron camtschaticum*) to serve as outgroups. Two phylogenetic approaches were used: the maximum likelihood (ML) method and the neighbor-joining (NJ) method. IQ-TREE (version 2.3.4) was used to construct the ML tree with 1000 bootstrap replicates, while MEGA12 was used to build the NJ tree with 1000 bootstrap replicates. Genes that consistently clustered with known olfactory receptors in both analyses were ultimately identified as olfactory receptor genes.

Cross-species analysis

To compare the cellular and transcriptional profiles during regeneration across different species, scRNA-seq datasets were analyzed from five model organisms: *Xenopus laevis* (*70*), *D. rerio* (*71*), *Schmidtea mediterranea* (*72*), *H. vulgaris* (*18*), and *Hofstenia miamia* (*73*). Using the SAMap pipeline (*74*), cell-to-cell similarity matrices were generated between *A. coerulea* and each of these species. To enable cross-species integrative gene expression analysis, based on a SAMap-derived matrix of homologous genes, genes from each species were unified and

mapped to the *A. coerulea* gene nomenclature. On this basis, cross-species single-cell datasets were subsequently integrated to construct a unified expression matrix for downstream comparative analyses. Single-cell data from the lizard *Anolis carolinensis* (*75*) were further incorporated to investigate gene expression dynamics during blastema formation.

Pharmacological treatment

For the Wnt pathway inhibition experiment, 12 medusae (2 to 3 cm in diameter) were assigned to two groups: a control group cultured in 100 ml of FASW containing 100 μL DMSO and an inhibitor-treated group cultured in 100 ml of FASW containing 1000 nM of the Wnt signaling pathway inhibitor IWP2 (*32*). Before injury, both groups were pretreated for 24 hours. Half of the rhopalia in each medusa were then surgically removed using a sterile scalpel, and morphological regeneration was assessed under a microscope at 72 hours post-amputation. All treatment groups were cultured at 15°C with orbital shaking at orbital shaking at 50 revolutions per minute (rpm), and the medium was replaced every 24 hours.

For the RA signaling intervention experiment, the medusae were divided into three groups: a DMSO control group, an RA synthesis inhibition group (DEAB), and an RA rescue group (DEAB + RA). Each group contained 10 medusae that were subjected to rhopalia removal and cultured in FASW for 2 days postamputation to allow blastema formation. Medusae in the DEAB and DEAB + RA groups were immersed in 100 ml of FASW containing 10 μM DEAB, a retinaldehyde dehydrogenase inhibitor that blocks endogenous RA synthesis (*38*); the rescue group additionally received 0.5 μM all-trans RA. All pharmacological treatments were initiated at day 2 postinjury (corresponding to the blastema formation stage) and maintained for 72 hours under controlled conditions (15°C, orbital shaking at 50 rpm), with the 100-ml treatment solutions replaced every 24 hours. The regeneration of ocelli and statocysts was examined and quantified daily under a microscope.

To further verify the specificity of the pharmacological intervention, we applied an identical treatment protocol as described previously to the samples, collected tissues from the regenerative area at the rhopalium amputation site to prepare single-cell suspensions, and then used a calcein-AM/PI double-staining kit (Solarbio Biotech, China) to assess the viability of dissociated single cells in strict accordance with the manufacturer's operating instruction. Dunn's test was applied for multiple pairwise comparisons between groups.

To assess the role of RA in normal rhopalial development, polyps were cultured in FASW under three treatment conditions: A vehicle control containing 5 μM 5-methoxy-2-methyl indole dissolved in DMSO, a low-dose RA treatment containing 1 μM RA and 5 μM 5-methoxy-2-methyl indole, and a high-dose RA treatment containing 2.5 μM RA and 5 μM 5-methoxy-2-methyl indole. 5-Methoxy-2-methyl indole was used to induce the metamorphic transition from polyps to ephyrae (*24*). For each treatment, 48 healthy polyps of comparable size were individually cultured in 48-well cell culture plates (one polyp per well) with 1 ml of the corresponding treatment solution per well and maintained at 15°C. Treatment solutions were renewed daily, and statocyst formation was monitored and recorded on a daily basis. Newly released ephyrae were examined to quantify the number of ocelli under a microscope.

Reverse transcription quantitative PCR

Samples derived from the different treatment groups were collected for RNA extraction. cDNA was synthesized using the One-Step gDNA Removal and cDNA Synthesis SuperMix Kit (TransGen Biotech, Beijing, China), with strict adherence to the manufacturer's instructions. Quantitative PCR was performed using the SYBR Green Master Mix (Thermo Fisher Scientific) and an Applied Biosystems 7500 real-time PCR system (Foster City, CA, USA). All primers (sequences provided in table S3) were diluted to 10 pmol/liter. Each analysis was performed with at least three replicates. All samples were analyzed using *Gadph* as a reference gene. Expression was quantified using the ΔΔCt method. Statistical significance between groups was evaluated using two-tailed Student's *t* tests.

Whole-mount in situ and fluorescence in situ hybridization

Aurelia riboprobes (primer sequences provided in table S4) generated from templates produced via standard cloning and restriction endonuclease digestion were synthesized using a DIG RNA Labeling Kit (SP6/T7) (Roche, Basel, Switzerland). Riboprobes generated from templates produced via standard cloning and restriction digest were synthesized using the HighYield T7 AF555 RNA Labeling Kit (Jena Bioscience, Germany). Colorimetric in situ hybridization and fluorescence in situ were performed as described by Fuchs *et al.* (*76*) and Fujita *et al.* (*77*), with minor modifications. In brief, *A. coerulea* specimens were relaxed in 2% $MgCl_2$ for 10 min and fixed overnight at 4°C in 4% paraformaldehyde. The specimens were then dehydrated in a 25/50/75% methanol series for 20 min to remove undesired pigmentation and stored in 100% methanol at −20°C. The samples were rehydrated using a 75/50/25% methanol series for 10 min each, washed with PBT (phosphate buffer containing 0.05% Tween 20) for 10 min, and bleached in 3% H_2O_2/PBT solution for 10 min. The specimens were then permeabilized for 20 min with proteinase K (1 μg/ml; Sigma-Aldrich, St. Louis, MO, USA) in PBT. Hybridization was performed at 57°C for 72 hours in hybridization buffer [50% formamide, 5× SSC, 0.1% Tween-20, 0.1% CHAPS, 1× Denhardt's solution, and heparin (100 μg/ml) in DEPC water] with torula yeast RNA (0.5 mg/ml; Sigma-Aldrich). The samples were incubated with AP-conjugated anti-digoxigenin antibody (Roche) and detected with NBT/BCIP substrate using a DIG Nucleic Acid Detection Kit (Roche). Last, the samples were transferred to 80% glycerol and imaged using a DMi8 microscope (Leica, Wetzlar, Germany).

Supplementary Materials

The PDF file includes:

Figs. S1 to S14
Tables S1 to S4

Other Supplementary Material for this manuscript includes the following:

Dataset S1

REFERENCES

1. K. D. Poss, Advances in understanding tissue regenerative capacity and mechanisms in animals. *Nat. Rev. Genet.* **11**, 710–722 (2010).
2. F. Cebrià, Regenerating the central nervous system: How easy for planarians! *Dev. Genes Evol.* **217**, 733–748 (2007).
3. V. V. Kozin, N. A. Filippova, R. P. Kostyuchenko, Regeneration of the nervous and muscular system after caudal amputation in the polychaete *Alitta virens* (Annelida: Nereididae). *Russ. J. Dev. Biol.* **48**, 198–210 (2017).
4. V. S. Mashanov, O. R. Zueva, T. Heinzeller, Regeneration of the radial nerve cord in a holothurian: A promising new model system for studying post-traumatic recovery in the adult nervous system. *Tissue Cell* **40**, 351–372 (2008).
5. F. Rentzsch, M. Layden, M. Manuel, The cellular and molecular basis of cnidarian neurogenesis. *Wiley Interdiscip. Rev. Dev. Biol.* **6**, e257 (2017).
6. P. J. Horner, F. H. Gage, Regenerating the damaged central nervous system. *Nature* **407**, 963–970 (2000).

7. E. M. Tanaka, P. Ferretti, Considering the evolution of regeneration in the central nervous system. *Nat. Rev. Neurosci.* **10**, 713–723 (2009).
8. A. X. Sun, R. Londono, M. L. Hudnall, R. S. Tuan, T. P. Lozito, Differences in neural stem cell identity and differentiation capacity drive Divergent regenerative outcomes in lizards and salamanders. *Proc. Natl. Acad. Sci. U.S.A.* **115**, E8256–E8265 (2018).
9. W. Wang, C.-K. Hu, A. Zeng, D. Alegre, D. Hu, K. Gotting, A. Ortega Granillo, Y. Wang, S. Robb, R. Schnittker, S. Zhang, D. Alegre, H. Li, E. Ross, N. Zhang, A. Brunet, A. Sánchez Alvarado, Changes in regeneration-responsive enhancers shape regenerative capacities in vertebrates. *Science* **369**, eaaz3090 (2020).
10. A. Zeng, H. Li, L. Guo, X. Gao, S. McKinney, Y. Wang, Z. Yu, J. Park, C. Semerad, E. Ross, L.-C. Cheng, E. Davies, K. Lei, W. Wang, A. Perera, K. Hall, A. Peak, A. Box, A. Sánchez Alvarado, Prospectively isolated Tetraspanin$^+$ neoblasts are adult pluripotent stem cells underlying planaria regeneration. *Cell* **173**, 1593–1608.e20 (2018).
11. M. C. Vogg, B. Galliot, C. D. Tsiairis, Model systems for regeneration: *Hydra*. *Development* **146**, dev177212 (2019).
12. T. Katsuki, R. J. Greenspan, Jellyfish nervous systems. *Curr. Biol.* **23**, R592–R594 (2013).
13. T. C. G. Bosch, A. Klimovich, T. Domazet-Lošo, S. Gründer, T. W. Holstein, G. Jékely, D. J. Miller, A. P. Murillo-Rincon, F. Rentzsch, G. S. Richards, K. Schröder, U. Technau, R. Yuste, Back to the basics: Cnidarians start to fire. *Trends Neurosci.* **40**, 92–105 (2017).
14. A. Garm, P. Ekstrom, M. Boudes, D. E. Nilsson, Rhopalia are integrated parts of the central nervous system in box jellyfish. *Cell. Tissue. Res.* **325**, 333–343 (2006).
15. S. A. Stamatis, K. Worsaae, A. Garm, Regeneration of the rhopalium and the rhopalial nervous system in the box jellyfish *Tripedalia cystophora*. *Biol. Bull.* **234**, 22–36 (2018).
16. L. S. Wyss, S. R. Bray, B. Wang, Cellular diversity and developmental hierarchy in the planarian nervous system. *Curr. Opin. Genet. Dev.* **76**, 101960 (2022).
17. P. Álvarez-Campos, H. García-Castro, E. Emili, A. Pérez-Posada, I. Del Olmo, S. Peron, D. A. Salamanca-Díaz, V. Mason, B. Metzger, A. E. Bely, N. J. Kenny, B. D. Özpolat, J. Solana, Annelid adult cell type diversity and their pluripotent cellular origins. *Nat. Commun.* **15**, 3194 (2024).
18. S. Siebert, J. A. Farrell, J. F. Cazet, Y. Abeykoon, A. S. Primack, C. E. Schnitzler, C. E. Juliano, Stem cell differentiation trajectories in Hydra resolved at single-cell resolution. *Science* **365**, eaav9314 (2019).
19. D. A. Gold, D. K. Jacobs, Stem cell dynamics in Cnidaria: Are there unifying principles? *Dev. Genes. Evol.* **223**, 53–66 (2013).
20. E. M. De Robertis, Wnt signaling in axial patterning and regeneration: Lessons from planaria. *Sci. Signal.* **3**, pe21 (2010).
21. P. W. Reddien, A. L. Bermange, A. M. Kicza, A. S. Alvarado, BMP signaling regulates the dorsal planarian midline and is needed for asymmetric regeneration. *Development* **134**, 4043–4051 (2007).
22. L. Todd, L. Suarez, C. Quinn, A. J. Fischer, Retinoic acid-signaling regulates the proliferative and neurogenic capacity of Müller glia-derived progenitor cells in the avian retina. *Stem Cells* **36**, 392–405 (2018).
23. W. Zhang, P. Luo, X. Liu, R. Cheng, S. Zhang, X. Qian, F. Liu, Roles of fibroblast growth factors in the axon guidance. *Int. J. Mol. Sci.* **24**, 10292 (2023).
24. Z. Dong, F. Wang, Y. Liu, Y. Li, H. Yu, S. Peng, T. Sun, M. Qu, K. Sun, L. Wang, Y. Ma, K. Chen, J. Zhao, Q. Lin, Genomic and single-cell analyses reveal genetic signatures of swimming pattern and diapause strategy in jellyfish. *Nat. Commun.* **15**, 5936 (2024).
25. D. A. Gold, T. Katsuki, Y. Li, X. Yan, M. Regulski, D. Ibberson, T. Holstein, R. E. Steele, D. K. Jacobs, R. J. Greenspan, The genome of the jellyfish *Aurelia* and the evolution of animal complexity. *Nat. Ecol. Evol.* **3**, 96–104 (2019).
26. J. Takouda, S. Katada, T. Imamura, T. Sanosaka, K. Nakashima, *SoxE* group transcription factor *Sox8* promotes astrocytic differentiation of neural stem/precursor cells downstream of Nfia. *Pharmacol. Res. Perspect.* **9**, e00749 (2021).
27. A. Alié, L. Leclère, M. Jager, C. Dayraud, P. Chang, H. Le Guyader, E. Quéinnec, M. Manuel, Somatic stem cells express *Piwi* and *Vasa* genes in an adult ctenophore: Ancient association of "germline genes" with stemness. *Dev. Biol.* **350**, 183–197 (2011).
28. Y. Yang, N. Gomez, N. Infarinato, R. C. Adam, M. Sribour, I. Baek, M. Laurin, E. Fuchs, The pioneer factor *SOX9* competes for epigenetic factors to switch stem cell fates. *Nat. Cell Biol.* **25**, 1185–1195 (2023).
29. Y. Liu, C. Huang, M. Bai, C. Pi, D. Zhang, J. Xie, The roles of *Runx1* in skeletal development and osteoarthritis: A concise review. *Heliyon* **8**, e12656 (2022).
30. C. Y. Lin, W. T. Chen, H. C. Lee, P. H. Yang, H. J. Yang, H. J. Tsai, The transcription factor *Six1a* plays an essential role in the craniofacial myogenesis of zebrafish. *Dev. Biol.* **331**, 152–166 (2009).
31. J. C. Holstege, W. de Graaff, M. Hossaini, S. Cardona Cano, D. Jaarsma, E. van den Akker, J. Deschamps, Loss of *Hoxb8* alters spinal dorsal laminae and sensory responses in mice. *Proc. Natl. Acad. Sci. U.S.A.* **105**, 6338–6343 (2008).
32. B. García-Reyes, L. Witt, B. Jansen, E. Karasu, T. Gehring, J. Leban, D. Henne-Bruns, C. Pichlo, E. Brunstein, U. Baumann, F. Wesseler, B. Rathmer, D. Schade, C. Peifer, U. Knippschild, Discovery of inhibitor of Wnt production 2 (IWP-2) and related compounds as selective ATP-competitive inhibitors of casein kinase 1 (CK1) δ/ε. *J. Med. Chem.* **61**, 4087–4102 (2018).
33. B. A. Upton, N. M. Díaz, S. A. Gordon, R. N. Van Gelder, E. D. Buhr, R. A. Lang, Evolutionary constraint on visual and nonvisual mammalian opsins. *J. Biol. Rhythms* **36**, 109–126 (2021).
34. M. N. Moraes, L. V. M. de Assis, I. Provencio, A. M. D. Castrucci, Opsins outside the eye and the skin: A more complex scenario than originally thought for a classical light sensor. *Cell. Tissue. Res.* **385**, 519–538 (2021).
35. C. Cai, X. Hu, P. Dai, T. Zhang, M. Jiang, L. Wang, W. Hua, Y. Fan, X. X. Han, Z. Gao, c-Myc regulates neural stem cell quiescence and activation by coordinating the cell cycle and mitochondrial remodeling. *Signal. Transduct. Target. Ther.* **6**, 306 (2021).
36. B. Huang, X. Li, X. Tu, W. Zhao, D. Zhu, Y. Feng, X. Si, J. G. Chen, *OTX1* regulates cell cycle progression of neural progenitors in the developing cerebral cortex. *J. Biol. Chem.* **293**, 2137–2148 (2018).
37. R. Doi, M. Endo, K. Yamakoshi, Y. Yamanashi, M. Nishita, S. Fukada, Y. Minami, Critical role of Frizzled1 in age-related alterations of Wnt/β-catenin signal in myogenic cells during differentiation. *Genes Cells* **19**, 287–296 (2014).
38. X. Ma, P. Zhu, Y. Ding, H. Zhang, Q. Qiu, A. V. Dvornikov, Z. Wang, M. Kim, Y. Wang, M. Lowerison, Y. Yu, N. Norton, J. Herrmann, S. C. Ekker, T. K. Hsiai, X. Lin, X. Xu, Retinoid X receptor alpha is a spatiotemporally predominant therapeutic target for anthracycline-induced cardiotoxicity. *Sci. Adv.* **6**, eaay2939 (2020).
39. R. Yang, F. Ji, J. Jiao, Early central nervous system development and neuron regeneration. *Curr. Opin. Genet. Dev.* **90**, 102286 (2025).
40. A. D. Zhao, H. Qin, X. B. Fu, What determines the regenerative capacity in animals? *Bioscience* **66**, 735–746 (2016).
41. G. J. Romanes, Further observations on the locomotor system of medusae. *Proc. R. Soc. Lond.* **25**, 464–487 (1877).
42. P. W. Reddien, Specialized progenitors and regeneration. *Development* **140**, 951–957 (2013).
43. J. M. Gahan, B. Bradshaw, H. Flici, U. Frank, The interstitial stem cells in *Hydractinia* and their role in regeneration. *Curr. Opin. Genet. Dev.* **40**, 65–73 (2016).
44. C. E. Juliano, A. Reich, N. Liu, J. Götzfried, M. Zhong, S. Uman, R. A. Reenan, G. M. Wessel, R. E. Steele, H. Lin, PIWI proteins and PIWI-interacting RNAs function in *Hydra* somatic stem cells. *Proc. Natl. Acad. Sci. U.S.A.* **111**, 337–342 (2014).
45. A. Denner, J. Steger, A. Ries, E. Morozova-Link, J. Ritter, F. Haas, A. G. Cole, U. Technau, *Nanos2* marks precursors of somatic lineages and is required for germline formation in the sea anemone *Nematostella vectensis*. *Sci. Adv.* **10**, eado0424 (2024).
46. C. P. Petersen, P. W. Reddien, A wound-induced Wnt expression program controls planarian regeneration polarity. *Proc. Natl. Acad. Sci. U.S.A.* **106**, 17061–17066 (2009).
47. D. Wehner, W. Cizelsky, M. D. Vasudevaro, G. Ozhan, C. Haase, B. Kagermeier-Schenk, A. Röder, R. I. Dorsky, E. Moro, F. Argenton, M. Kühl, G. Weidinger, Wnt/β-catenin signaling defines organizing centers that orchestrate growth and differentiation of the regenerating zebrafish caudal fin. *Cell Rep.* **6**, 467–481 (2014).
48. H. Yokoyama, H. Ogino, C. L. Stoick-Cooper, R. M. Grainger, R. T. Moon, Wnt/β-catenin signaling has an essential role in the initiation of limb regeneration. *Dev. Biol.* **306**, 170–178 (2007).
49. M. van Wyk, S. Kleinlogel, A visual opsin from jellyfish enables precise temporal control of G protein signalling. *Nat. Commun.* **14**, 2450 (2023).
50. N. Picciani, C. A. Berger, S. Nielsen, J. Musser, A. P. Oel, M. I. Stoilova, D. Arendt, A. Garm, T. H. Oakley, Comparative analysis of convergent jellyfish eyes reveals extensive differences in expression of vision-related genes. *Ecol. Evol.* **15**, e71784 (2025).
51. G. Bennetti, A. Corbin-Leftwich, L. M. Boland, I. Skromne, Retinoic acid inhibition impairs planarian eye regeneration. *Neurosci. J.* **16**, 1–8 (2019).
52. O. N. Ermakova, A. M. Ermakov, K. P. Tiras, V. V. Lednev, Retinoic acid as a regulator of planarian morphogenesis. *Ontogenez* **40**, 367–372 (2009).
53. N. Papalopulu, J. D. Clarke, L. Bradley, D. Wilkinson, R. Krumlauf, N. Holder, Retinoic acid causes abnormal development and segmental patterning of the anterior hindbrain in *Xenopus* embryos. *Development* **113**, 1145–1158 (1991).
54. N. Holder, J. Hill, Retinoic acid modifies development of the midbrain-hindbrain border and affects cranial ganglion formation in zebrafish embryos. *Development* **113**, 1159–1170 (1991).
55. W. Lin, X. Jia, X. Shi, Q. He, P. Zhang, X. Zhang, L. Zhang, M. Wu, T. Ren, Y. Liu, H. Deng, Y. Li, S. Liu, S. Huang, J. Kang, J. Luo, Z. Deng, W. Wang, Reactivation of mammalian regeneration by turning on an evolutionarily disabled genetic switch. *Science* **388**, eadp0176 (2025).
56. J. Singh, M. R. Randle, B. J. Walters, B. C. Cox, The transcription factor *Pou4f3* is essential for the survival of postnatal and adult mouse cochlear hair cells and normal hearing. *Front. Cell. Neurosci.* **18**, 1369282 (2024).
57. S. Li, A. Mecca, J. Kim, G. A. Caprara, E. L. Wagner, T.-T. Du, L. Petrov, W. Xu, R. Cui, I. T. Rebustini, B. Kachar, A. W. Peng, J.-B. Shin, Myosin-VIIa is expressed in multiple isoforms and essential for tensioning the hair cell mechanotransduction complex. *Nat. Commun.* **11**, 2066 (2020).
58. H. Chen, C. Cretu, A. Trebilcock, N. Evdokimova, N. Babai, L. Feldmann, F. Leidner, F. Benseler, S. Mutschall, K. Esch, C. Z. K. Szabo, V. Pena, C. Pape, H. Grubmüller,

N. Strenzke, N. Brose, C. Wichmann, J. Preobraschenski, T. Moser, Structure and function of otoferlin, a synaptic protein of sensory hair cells essential for hearing. *Sci. Adv.* **11**, eady8532 (2025).
59. Y. C. Chuang, C. H. Lee, W. H. Sun, C. C. Chen, Involvement of advillin in somatosensory neuron subtype-specific axon regeneration and neuropathic pain. *Proc. Natl. Acad. Sci. U.S.A.* **115**, E8557–E8566 (2018).
60. J. Bielecki, G. Nachman, A. Garm, Swim pacemaker response to bath applied neurotransmitters in the cubozoan *Tripedalia cystophora*. *J. Comp. Physiol. A Neuroethol. Sens. Neural Behav. Physiol.* **199**, 785–797 (2013).
61. R. T. Hayward, "Modeling experiments on pacemaker interactions in scyphomedusae", Master's thesis, University of North Carolina at Wilmington, Department of Biology and Marine Biology, Wilmington, NC (2009).
62. L. Kumar, M. E. Futschik, Mfuzz: A software package for soft clustering of microarray data. *Bioinformation* **2**, 5–7 (2007).
63. S. Hänzelmann, R. Castelo, J. Guinney, GSVA: Gene set variation analysis for microarray and RNA-seq data. *BMC Bioinformatics* **14**, 7 (2013).
64. G. C. Yu, L. G. Wang, Y. Y. Han, Q. Y. He, ClusterProfiler: An R package for comparing biological themes among gene clusters. *Omics* **16**, 284–287 (2012).
65. C. S. McGinnis, L. M. Murrow, Z. J. Gartner, DoubletFinder: Doublet detection in single-cell RNA sequencing data using artificial nearest neighbors. *Cell Syst.* **8**, 329–337.e4 (2019).
66. J. Cao, M. Spielmann, X. Qiu, X. Huang, D. M. Ibrahim, A. J. Hill, F. Zhang, S. Mundlos, L. Christiansen, F. J. Steemers, C. Trapnell, J. Shendure, The single-cell transcriptional landscape of mammalian organogenesis. *Nature* **566**, 496–502 (2019).
67. K. Street, D. Risso, R. B. Fletcher, D. Das, J. Ngai, N. Yosef, E. Purdom, S. Dudoit, Slingshot: Cell lineage and pseudotime inference for single-cell transcriptomics. *BMC Genomics* **19**, 477 (2018).
68. X. Qiu, Q. Mao, Y. Tang, L. Wang, R. Chawla, H. A. Pliner, Reversed graph embedding resolves complex single-cell trajectories. *Nat. Methods* **14**, 979–982 (2017).
69. S. Jin, C. F. Guerrero-Juarez, L. Zhang, I. Chang, R. Ramos, C.-H. Kuan, P. Myung, M. V. Plikus, Q. Nie, Inference and analysis of cell-cell communication using CellChat. *Nat. Commun.* **12**, 1088 (2021).
70. C. Aztekin, T. W. Hiscock, J. C. Marioni, J. B. Gurdon, B. D. Simons, J. Jullien, Identification of a regeneration-organizing cell in the *Xenopus* tail. *Science* **364**, 653–658 (2019).
71. Y. Hou, H. J. Lee, Y. Chen, J. Ge, F. O. I. Osman, A. R. McAdow, M. H. Mokalled, S. L. Johnson, G. Zhao, T. Wang, Cellular diversity of the regenerating caudal fin. *Sci. Adv.* **6**, eaba2084 (2020).
72. M. L. Scimone, J. K. Cloutier, C. L. Maybrun, P. W. Reddien, The planarian wound epidermis gene equinox is required for blastema formation in regeneration. *Nat. Commun.* **13**, 2726 (2022).
73. R. E. Hulett, J. O. Kimura, D. M. Bolaños, Y.-J. Luo, C. Rivera-López, L. Ricci, M. Srivastava, Acoel single-cell atlas reveals expression dynamics and heterogeneity of adult pluripotent stem cells. *Nat. Commun.* **14**, 2612 (2023).
74. A. J. Tarashansky, J. M. Musser, M. Khariton, P. Li, D. Arendt, S. R. Quake, B. Wang, Mapping single-cell atlases throughout Metazoa unravels cell type evolution. *eLife* **10**, e66747 (2021).
75. A. C. Vonk, X. Zhao, Z. Pan, M. L. Hudnall, C. G. Oakes, G. A. Lopez, S. C. Hasel-Kolossa, A. W. C. Kuncz, S. B. Sengelmann, D. J. Gamble, T. P. Lozito, Single-cell analysis of lizard blastema fibroblasts reveals phagocyte-dependent activation of Hedgehog-responsive chondrogenesis. *Nat. Commun.* **14**, 4489 (2023).
76. B. Fuchs, W. Wang, S. Graspeuntner, Y. Li, S. Insua, E. M. Herbst, P. Dirksen, A. M. Böhm, G. Hemmrich, F. Sommer, T. Domazet-Lošo, U. C. Klostermeier, F. Anton-Erxleben, P. Rosenstiel, T. C. G. Bosch, K. Khalturin, Regulation of polyp-to-jellyfish transition in *Aurelia aurita*. *Curr. Biol.* **24**, 263–273 (2014).
77. S. Fujita, M. Takahashi, G. Kumano, E. Kuranaga, M. Miura, Y. I. Nakajima, Distinct stem-like cell populations facilitate functional regeneration of the Cladonema medusa tentacle. *PLOS Biol.* **21**, e3002435 (2023).

Acknowledgments: We thank the advice from K. Chen in scRNA-seq and analysis. We are grateful for resources from the High-Performance Computing Platform of Yantai Institute of Coastal Zone Research, Chinese Academy of Sciences. **Funding:** This work was supported by the National Science & Technology Fundamental Resources Investigation Program of China 2022FY100600 (Z.D.), National Key Research and Development Program of China 2023YFC3108200 (Z.D., L.W., and J.Z.), Key Project of the NSFC-Shandong Joint Fund U2106208 (Z.D.), and Taishan Scholars Program tsqn202211263 (Z.D.). **Author contributions:** Conceptualization: Z.D. Methodology: Y.L., T.S., X.M., Z.Y., Z.X., and L.W. Investigation: Y.L., T.S., X.M., Z.Y., F.W., Z.X., W.W., and Y.X. Visualization: Y.L., F.W., Z.Y., T.S., and S.P. Supervision: Z.D. and J.Z. Funding acquisition: Z.D. Writing–original draft: Y.L., F.W., and Z.D. Writing–review and editing: Y.L., F.W., and Z.D. **Competing interests:** The authors declare that they have no competing interests. **Data, code, and materials availability:** Sequencing data have been deposited in the NCBI under BioProject accession number PRJNA1224934. All other data needed to evaluate and reproduce the results in the paper are present in the paper and/or the Supplementary Materials. The processed files and code are publicly available in Zenodo at https://doi.org/10.5281/zenodo.19466460. This study did not generate new materials.

Submitted 26 August 2025
Accepted 14 April 2026
Published 20 May 2026
10.1126/sciadv.aeb8034